

Hydrogen Bond-Enabled High-ICE Anode for Lithium-Ion Battery Using Carbonized Citric Acid-Coated Silicon Flake in PAA Binder

Yonhua Tzeng,* Cheng-Ying Jhan, Guan-Yu Chen, Kuo-Ming Chiu, Yi-Chen Wu, and Pin-Sen Wang

Cite This: *ACS Omega* 2023, 8, 8001–8010

Read Online

ACCESS |



Metrics & More

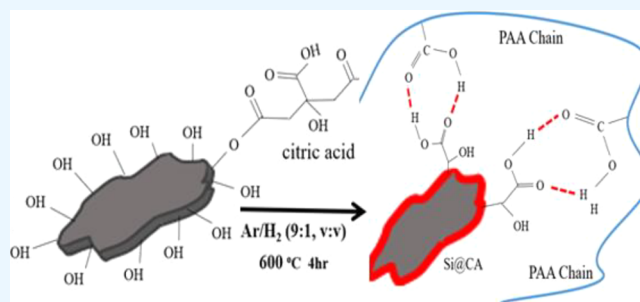


Article Recommendations



Supporting Information

ABSTRACT: A silicon-based lithium-ion battery (LIB) anode is extensively studied because of silicon's abundance, high theoretical specific capacity (4200 mAh/g), and low operating potential versus lithium. Technical barriers to large-scale commercial applications include the low electrical conductivity and up to about 400% volume changes of silicon due to alloying with lithium. Maintaining the physical integrity of individual silicon particles and the anode structure is the top priority. We use strong hydrogen bonds between citric acid (CA) and silicon to firmly coat CA on silicon. Carbonized CA (CCA) enhances electrical conductivity of silicon. Polyacrylic acid (PAA) binder encapsulates silicon flakes by strong bonds formed by abundant COOH functional groups in PAA and silicon particles and the whole anode. The silicon-based anode shows high initial coulombic efficiency, around 90%, and the capacity retention of 1479 mAh/g after 200 discharge–charge cycles at 1 A/g current. At 4 A/g, the capacity retention of 1053 mAh/g was achieved. A durable high-ICE silicon-based LIB anode capable of high discharge–charge current has been reported.



1. INTRODUCTION

When modern civilization evolves, demands for large-scale and efficient energy storage continue to increase. Fossil fuels cause environmental damages and are expected to gradually become exhaustive. Renewable energy brings hopes for a cleaner future.¹ However, solar power, wind power, hydraulic power, and so forth cannot supply energy continuously. Energy storage systems are therefore needed to store excessive energy for later uses. On the other hand, mobile devices including long-range electric vehicles require high-specific-capacity and long-cycling-life energy storage systems for retaining electricity storage capacity after repetitive discharge–charge cycling. A lithium-ion battery (LIB) is the most promising device to meet future demands. However, state-of-the-art LIB still leaves much room for improvement.

According to the long-term goal set by the U.S. Advanced Battery Consortium LLC (USABC), the energy density of 235 Wh k/g or 500 Wh/L at a discharge rate of 1/3 C, which means that a battery can be fully discharged in 3 h, is needed for a LIB pack.² Traditional LIBs of graphite versus lithium transition metal oxide cells are insufficient. Therefore, new electrode materials and chemistry, which can provide drastically higher energy density and excellent cycle stability, are crucial to next-generation batteries.^{3,4}

Among LIB anode materials, silicon is most promising because of its high theoretical capacity (3579 mAh/g, $\text{Li}_{15}\text{Si}_4$ at room temperature), which is about 10 times that of graphite.^{5,6} Silicon also has a relatively low discharge potential (~ 0.2 V vs Li/Li^+), which increases the overall energy density. Silicon is

the second most abundant element in the crust of the earth. It is inexpensive and stable. Chemical properties of silicon are relatively harmless to the environments and are not affected by solvent co-intercalation.⁷

The full lithiation of Si results in a large volume expansion of $\sim 400\%$ to active silicon particles. A novel means of preventing the volume expansion and stresses it induces from causing pulverization of silicon particles and cracks of silicon-based anode is needed. When an electron leaves a silicon particle, there has to be a positively charged lithium ion leaving the same silicon particle to maintain charge neutrality. The same happens to the arrival of an electron to a silicon particle along with a positively charged lithium ion. When a piece of crushed silicon particle loses electrical connection with the current collector, it loses the conductivity path for electrons between the silicon and the current collector and, therefore, also the charge–discharge capability.^{8,9} On the other hand, the electrolyte is consumed when it reacts with a fresh silicon surface, which is exposed due to the breaking of a silicon particle into multiple particles, to form a solid electrolyte interphase (SEI) before normal discharging–charging oper-

Received: December 8, 2022

Accepted: February 6, 2023

Published: February 15, 2023



ation is established. SEI is a lithium containing compound, which is a good transfer medium for lithium ions, but a poor conductor for electrons. Excessive and continuous consumption of lithium for SEI formation causes an increase in irreversible capacity and an increase in the thickness of SEI and the internal discharge–charge electrochemical impedance of the LIB.^{5,10} In a packaged LIB, continuous consumption of a limited amount of electrolyte and lithium shortens its cycling life.¹¹

Silicon-based anodes often resort to innovative silicon nanostructures in the forms of nanoparticles, nanowires, nanotubes, nanofilms, and so forth.^{12–14} Mechanical stress and strain generated during volume changes by charging and discharging cause less damages to nano-scaled silicon particles and structures than their larger counterparts. The small bulk-to-surface ratio of the number of silicon atoms in a nanoscale silicon particle and additional buffer space provided in a silicon-based porous nanostructure are beneficial to the physical integrity of an active silicon particle in the anode. Nanostructured silicon materials exhibit large specific surface areas, short lithium-ion diffusion distance, and good electron transport ability, which are in favor of improved electrochemical performance of an anode. However, the large specific surface area of a silicon particle consumes more electrolyte for the formation of SEI on the silicon surface during the first discharge–charge cycle. A large portion of the consumed lithium is not released during the charging half cycle, resulting in the permanent loss of lithium and the undesirable low initial coulombic efficiency (ICE). The small contact area of a nanoscale silicon with the current collector may make its adhesion to the current collector challenging during volume changes.¹⁵ High costs for the fabrication of nanoscale silicon particles and silicon nanostructures add to undesirable barriers to commercial application of silicon-based anode for the LIB.

Porous anode structures provide room for the volume changes of silicon, reducing the stress it induces. A properly designed porous anode has a better chance of surviving repetitive lithiation and de-lithiation than a solid one. The short lithium ion diffusion distance for transport from the electrolyte to the silicon further allows high-current discharging and charging of a porous anode.^{16,17}

Composite materials, such as Si/C, Si/Graphene, and Si/SiC/C, have been reported to partially overcome volume expansion of silicon and the prevention of continuous SEI formation on a fresh silicon surface due to pulverization of silicon. Graphitic carbon coatings were found to be a good buffer and conductivity enhancement material, which reduces the probability of pulverization of silicon particles and enhances the physical integrity of the anode.^{18–21} In addition, suitable carbon coatings on silicon maintain the stability of the SEI and reduce continuous consumption of lithium for the formation of SEI. A properly designed silicon–carbon composite structure ensures strong bonding between the active electrode material and the current collector to increase the electrical conductivity of the anode.²² The pyrolytic or hot-pressed electrode converted part of the binder into conductive carbon and a carbon shell protective layer for silicon, thereby forming an effective conductive structure. This kind of electrode has a high ICE and excellent cycle stability. It is necessary to solve the problem of the binder losing its adhesive force with silicon after carbonization, which causes the powder to fall off.^{23–25} Electrospinning is a new nanofiber preparation technology. It produces nanofiber membrane characteristics of

a large specific surface area and high porosity, which provides multientry and short-range channel for metal ions to ensure a fast kinetics.^{26,27} Metal–organic frameworks have large specific surface areas, abundant pore structure, tunable compositions, and well-connected carbon matrices, which effectively ameliorate the huge volume variation, restrain the possible agglomeration in cycles, and also enhance the whole conductivity and the utilization of active storage sites.^{28–30}

Significant effects of a binder on the cycling performance of a silicon-based anode have been reported.^{31,32} A good binder provides firm bonding with and contacts among all active electrode materials, conductivity enhancing additives, and the current collector. It helps withstand the drastic volume changes of the electrode during battery cycling. Poly(acrylic acid) (PAA) is a polymer synthesized from acrylic monomers. It has a simple molecular structure and is easy to synthesize. Hydrogen bonds can be easily formed between the molecular chains of PAA and the active anode silicon particles due to the abundant carboxyl groups in PAA. Good affinity between PAA and active anode materials enhances the adhesion ability, which is beneficial to the physical integrity of the electrode.^{33,34} Tian et al. applied PAA binder to silicon-based anodes.³⁵ Results showed that the electrical performance of PAA-based anode is indeed better than those made with binders such as CMC and PVDF. This is attributed to the high density of carboxylic acid. The side chains of PAA have more COOH groups, which can form hydrogen bonds with Si-OH on the surface of silicon particles. It tightly wraps around a silicon particle and avoids cracks to form due to volume changes.³² The improved physical integrity of the anode and individual silicon particles by PAA minimizes the decomposition and deposition of electrolyte on the silicon surface.

For the purpose of maintaining the interfacial affinity between individual active silicon particles and the binder and at the same time enhancing the overall electrical conductivity of active silicon particles, in this work, silicon particles are coated by citric acid (Si@CA) using a sol–gel method. Heat treatment of citric acid results in a carbonized citric acid (CCA) coating that serves as a conductivity enhancement coating for silicon and a buffer layer to inhibit direct contacts between silicon particles and the electrolyte. Moreover, function groups on the CCA layer provide affinity with PAA. The strong dipole–dipole force avoids the detachment of a CCA-coated silicon particle from the PAA binder and provides self-healing effects to prolong the cycling life of the silicon-based anode. The combined effects enabled the achievements of high ICE and the retention of high capacity after long cycling.

2. EXPERIMENTAL SECTION

2.1. Chemicals. Silicon powder was provided by AUO Crystal Corporation in Taichung City, Taiwan, ROC, which was 100 nm in thickness and 800 nm in length and width. The silicon flakes came from silicon containing waste slurry generated from used silicon wafers. Battery-grade electrolyte, that is, 1 M LiPF₆ dissolved in equal volume of ethylene carbonate (EC), diethyl carbonate (DEC), dimethyl carbonate (DMC) with 10 wt % fluoroethylene carbonate (FEC) was purchased from Hopax Chemicals MFG. Co. in Taipei, Taiwan. Super P was obtained from Eubiq Technology Co in Taipei, Taiwan, as conductivity enhancement additives. PAA binder was provided by Eternal Materials Co in Tainan, Taiwan. To encapsulate the Si composites, the reagent

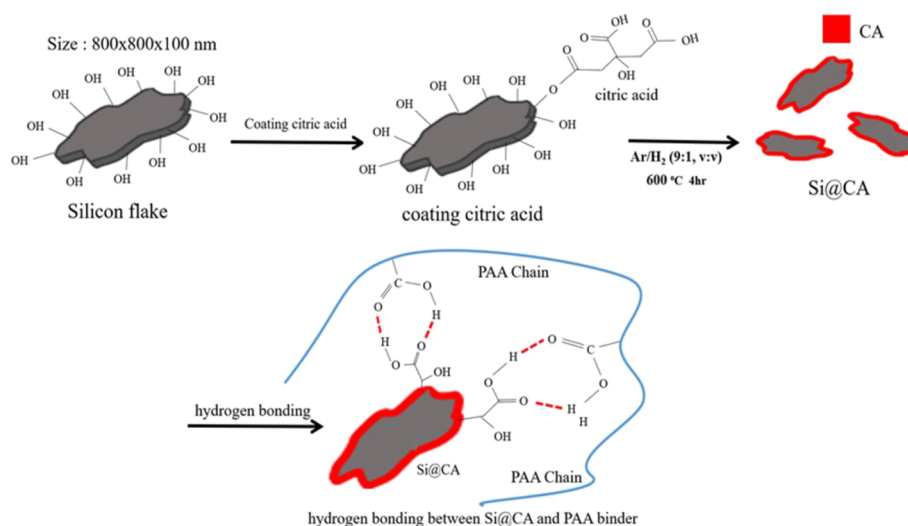


Figure 1. Schematic diagram of bonding between COOH groups on a silicon flake coated with carbonized citric acid and COOH groups of PAA binder.

including citric acid (99.5%, J.T. Baker) was used without further purification.

2.2. Preparation of the Si@CA Composites. For CCA-coated silicon flake (Si@CA), 2.5 g of Si and 6.25 g of citric acid were dissolved in ethanol and placed in a water bath at 60 °C with stirring overnight. After that, the solution was put into an oven for drying. For carbonization, the dried mixture was placed in a vacuum tube furnace at 600 °C for 4 h under an Ar/H₂ mixture atmosphere of Ar (90 vol %) and H₂ (10 vol %).

2.3. Fabrication of Coin Half Cells. Silicon flakes were mixed with conductivity enhancement additives, Super P, and PAA by the weight ratio of 70%:10%:20%, respectively. The slurry was stirred homogeneously and then applied on a 10 μm thick copper foil by means of a doctor blade. The thickness of the anode excluding the copper current collector was typically 15–20 μm. After the electrode was dried at 80 °C for 12 h, the electrode was cut into pieces of the diameter of 12 mm. The electrodes were put into an Ar-filled glove box with residual oxygen and moisture contents of less than 0.5 ppm to assemble the coin cells. Lithium metal was used as the counter/reference electrode. The electrolyte was 1 M LiPF₆ dissolved in equal volume of EC, DEC, and DMC with 10 wt % FEC. The mass loading for this work is 1.5 mg/cm.²

2.4. Materials Characterization. The morphology and structure of materials were examined by means of scanning electron microscopy (SEM, Hitachi-SU8000, Taipei, Taiwan) and scanning transmission electron microscopy (JEOL JEM-2100F Cs STEM, Taipei, Taiwan) with an acceleration voltage of 200 kV. A Horiba Scientific (Taipei, Taiwan) Raman system with a green laser at 532 nm and laser power at 450 mW was used to measure Raman spectra. The laser beam was focused on the sample surface in an area of about 10 μm in size. Raman spectra reveal the nanostructures of the sample. FTIR measurements were conducted on a Thermo/Nicolet, FTIR spectrometer (Thermo Fisher Scientific, Taipei, Taiwan) at room temperature under N₂ flow with a resolution of 4 cm⁻¹ and spectral range 650–4000 cm⁻¹. Attenuated total reflectance analysis was conducted with a Bruker Tensor equipped with a DTGS detector. All spectra were collected with 512 scans and spectral resolution of 4 cm⁻¹.

2.5. Electrode Characterization. The coin cells were disassembled in glove box after 200 discharge–charge cycles. Hereafter, the cycled electrodes were immersed in anhydrous DEC to remove residual electrolyte and then dried in a vacuum drier at 60 °C for 8 h. Using transmission electron microscopy (JEOL JEM-2100F Cs STEM, Taipei, Taiwan) and SEM (Hitachi-SU8000, Taipei, Taiwan), the morphology and structure of the cycled electrodes were characterized.

2.6. Test Cells. The charge–discharge cycling was analyzed by a battery testing system (BAT-750B). The cells were cycled at a voltage window between 0.01 and 1.50 V versus Li⁺/Li at 0.2 A/g for the first three cycles and 1.0 A/g for the following cycles. The specific capacity refers to the mAh per gram of silicon active material for the anode made of as-received silicon flake. For anode made of silicon flake coated with CCA coating, the specific capacity refers to the mAh per gram of the CCA-coated silicon flake in the anode.

Cyclic voltammetry (CV) and electrochemical impedance spectroscopy (EIS) were carried out using Autolab (Metrohm AUTOLAB BV, Taipei, Taiwan). The CV measurement used a scanning rate of 0.1 mV/s at room temperature. The EIS measurements were recorded in the frequency range of 0.01–100 kHz.

3. RESULTS AND DISCUSSION

Figure 1 shows a schematic diagram of bonding between COOH groups on CCA-coated Si flakes and COOH groups in PAA binder. Silicon flakes of the length and width of about 800 nm and the thickness of 100 nm were used. The OH groups on silicon flakes can generate hydrogen bonds with the carboxylic acid groups of the CA. There is good adhesion between silicon and CA. CA is carbonized to improve the electrical conductivity of the silicon flake and avoid direct contact between silicon flakes and the electrolyte. After carbonization, many COOH functional groups remain on the surface of the CCA coating,³⁶ which can generate hydrogen bonds with the carboxylic acid groups of the PAA binder. The good adhesion between the PAA and the active silicon material remains after the coating with CCA to provide both good electrical conductivity and physical integrity.

Figure 2 shows SEM images of as-received silicon flakes and those after coating with CCA. The lateral dimensions of the

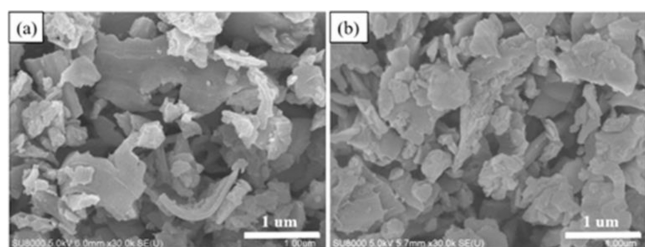


Figure 2. SEM images of (a) as-received Si flakes and (b) Si flakes coated with CCA (Si@CA).

silicon flakes are shown in the image to be on the order of 1 μm. In addition, the image of silicon flakes coated with CCA is not much different from that of the as-received silicon flakes.

Figure 3 shows (a,b) TEM images and (c–g) selected area electron diffraction (SAED) pattern and profiles of CCA-coated silicon flake (Si@CA). The silicon flake is covered by a 4–6 nm thick carbon layer. The SAED diffractograms confirm that the silicon flake is single crystalline. The measured inverted lattice phasor sizes from top to bottom are 6.081/nm, 3.191/nm, and 5.101/nm, corresponding to the d-spacing of silicon (3 1 1), (1 1 1), (2 2 0), which are 0.164, 0.313, and 0.196 nm, respectively.³⁷ The mappings show that the signal strength of C and O on the surface of the silicon flake is strong, and the intensity of these signals is mostly contributed by the residual functional groups of pyrolytic citric acid.

Figure 4 shows Raman spectra of (black) silicon flakes and (red) silicon flakes coated with CCA. The Raman peak at 510 cm^{-1} is from crystalline silicon.³⁸ The Si@CA samples are coated with CCA layers. Compared to the as-received silicon flakes, CCA coating exhibits two more characteristic peaks of the D-band at 1377 cm^{-1} and G-band at 1596 cm^{-1} . The ratio of signal intensity of the D-band to that of the G-band (I_D/I_G) for the Si@CA sample is 0.73. With the CCA coating, the Si@

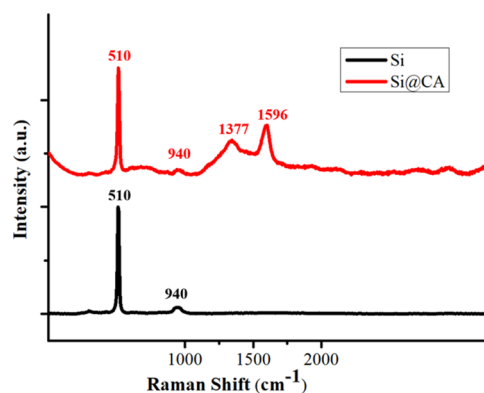


Figure 4. Raman spectra of Si flakes with carbonized CA coating (Si@CA) and as-received Si flakes.

CA samples exhibit the same crystalline silicon Raman signal at 510 cm^{-1} . The CA coating and the carbonization process did not cause damages to crystallinity of the silicon flake.

Unlike the pristine silicon flake with little carbon on the surface, an elemental analysis shows that the Si-flake@CA surface contains a carbon content of about 5 wt % of the total powder weight. This is consistent with the existence of CCA coatings on silicon flakes. The proportion of O is due to the fact that some COOH functional groups remained on the surface of Si@CA after pyrolysis. In addition, the atomic weight of H is too low to be accurately measured.

Figure 5 shows FTIR spectra of (a) as-received silicon flakes and silicon flakes coated with CCA and (b) the binder PAA and the binder PAA with CA additive. Surface functional groups on as-received silicon flakes and silicon flakes coated with CCA (Si@CA) are analyzed by FTIR. For the as-received silicon, a stretch vibrational peak of OySiH_x exists at 806 cm^{-1} , and asymmetric stretch absorption peaks of Si–O–Si exist at 1068 and 1227 cm^{-1} . There is a tensile absorption peak corresponding to 806 cm^{-1} OySiH_x at the wavenumber 2341 cm^{-1} . In addition, there is a broad Si–OH stretching peak in the range of wavenumbers 2988–3708 cm^{-1} . After silicon

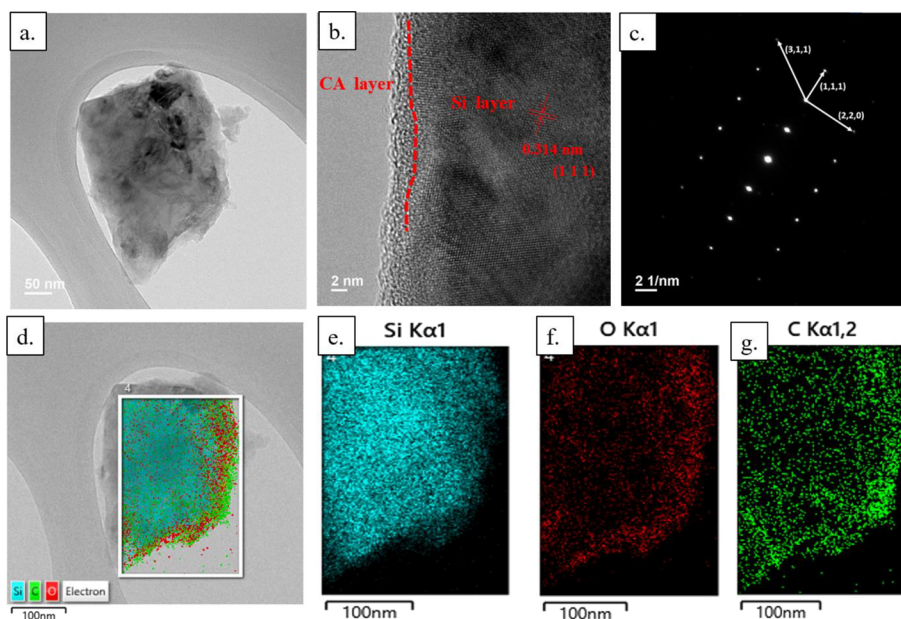


Figure 3. (a, b) TEM images and (c–g) selected area electron diffraction pattern and profiles of CCA-coated silicon flake (Si@CA).

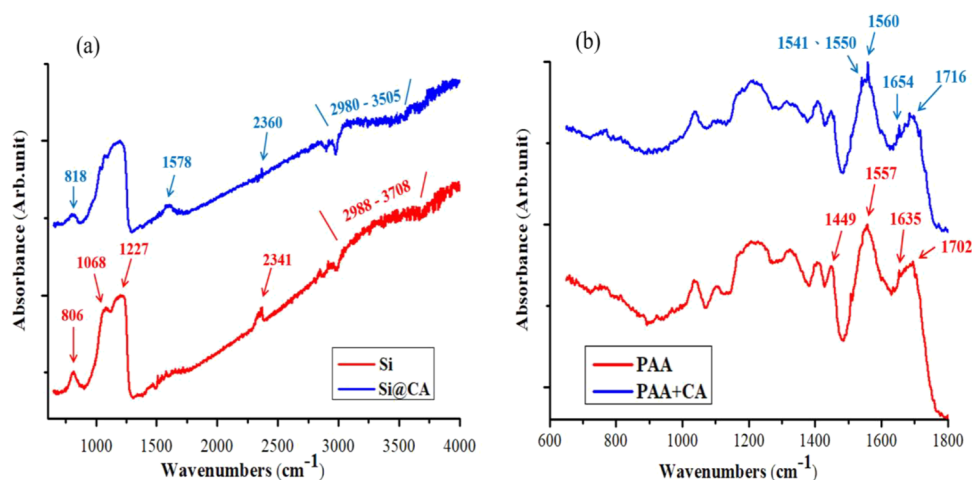


Figure 5. FTIR spectra of (a) Si flakes and carbonized CA-coated Si flakes (Si@CA) and (b) PAA and PAA with CA additive (PAA + CA).

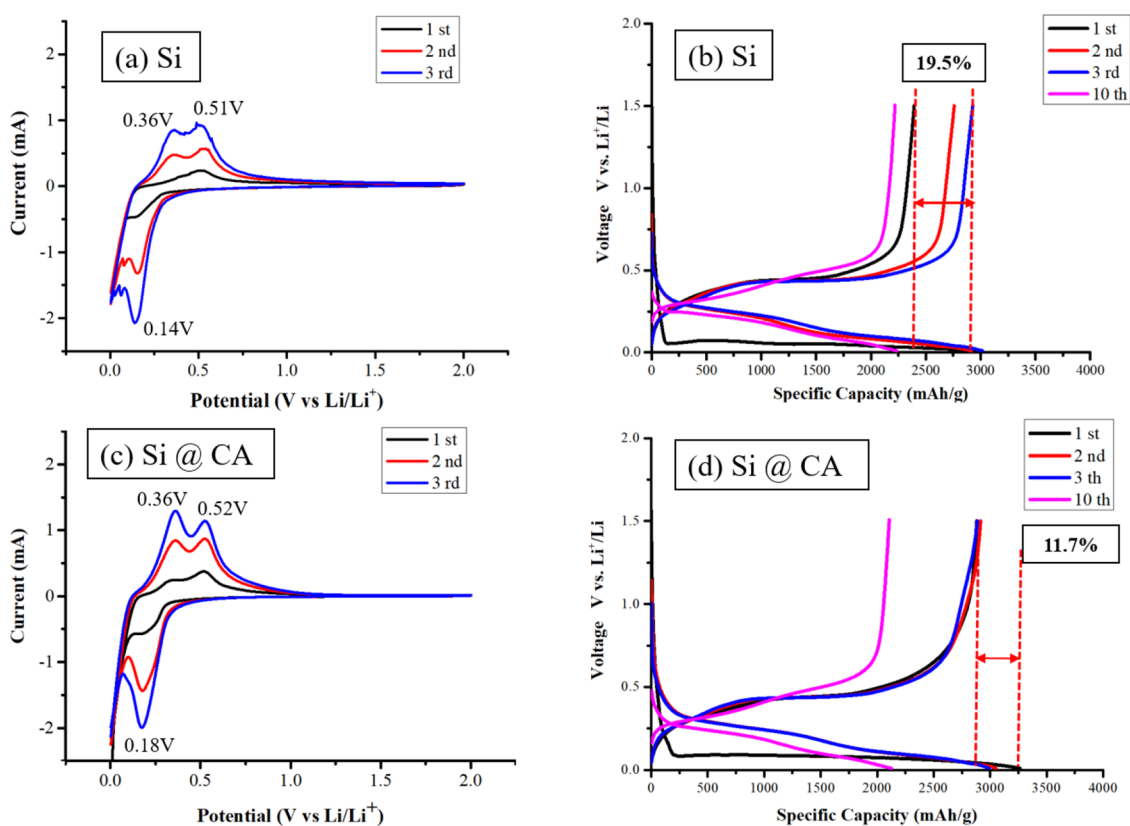


Figure 6. (a, c) Cyclic voltammetry and (b, d) voltage profile of anodes made of (a, b) Si flakes and (c, d) carbonized CA-coated silicon flakes (Si@CA).

flakes are coated by CCA, the stretch vibration peak of OySiHx that originally is located at 806 cm^{-1} shifts to 818 cm^{-1} . The relative intensity of the peak is also weakened. The stretching absorption peak of OySiHx has the same wavenumber at 2341 cm^{-1} , with its intensity being weaker than that from the as-received silicon. This may be attributed to interactions between the carboxylic acid groups on the surface of citric acid and the surface groups on the silicon flake. The $\text{C}=\text{O}$ tensile peak at the wavenumber of 1578 cm^{-1} is the characteristic peak of citric acid after heat treatment for carbonization. After being coated with citric acid, the original OH surface functional groups on the as-received silicon are replaced by the carboxylic acid groups. Due to the low

vibration frequency of the OH bond of the carboxylic acid group, the absorption peak appeared in the low wavenumber region. The OH group of the specimen shifts to the lower wavenumber in the range of $2980\text{--}3505\text{ cm}^{-1}$.^{39,40}

After carbonizing CA under the same conditions ($600\text{ }^\circ\text{C}$, $\text{Ar:H}_2 = 9:1$, 4 h), we made a mixture by a weight ratio of $\text{CA:PAA} = 1:9$. The solution was stirred overnight and dried for further analyzing the bonding forces of PAA and PAA with CA additive. FTIR profiling of PAA and PAA with CCA additive is shown in Figure 5b. In the FTIR spectrum of PAA, the stretching vibration peak of $\text{C}=\text{O}$ in COOH is at 1702 cm^{-1} . The absorption peak at 1635 cm^{-1} is attributed to the asymmetric stretching vibration of COO^- . The 1557 cm^{-1}

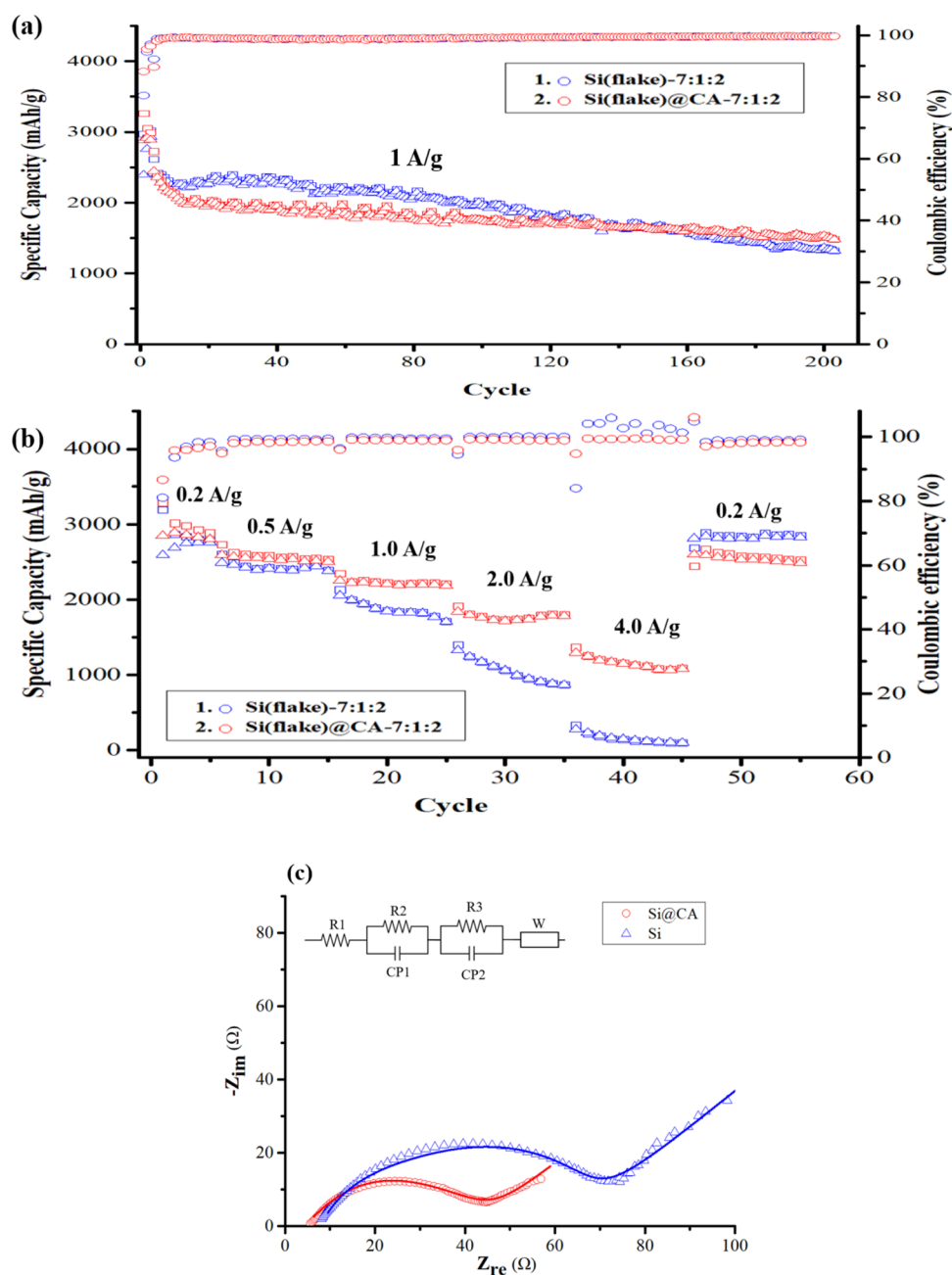


Figure 7. (a) Specific capacity cycling performance of anodes made of (1) (blue) silicon flakes and (2) (red) Si@CA; (b) cycling performance of anodes made of as-received silicon flakes and Si@CA at discharge–charge current ranging from 0.2 A/g (0.05 C) to 4 A/g (0.96 C); (c) electrochemical impedance spectra of the first cycle Si and Si@CA anode and the curve fitting equivalent circuit, where R1 represents the bulk resistance, (R2, CP1) and (R3, CP2) are the equivalent diffusion impedance, and W the Warburg element.

peak belongs to the stretching vibration peak of $\text{O}=\text{C}=\text{O}^-$. The absorption peak at 1449 cm^{-1} belongs to the symmetric stretching vibration of $-\text{COO}^-$. With CCA additive, the stretching vibration peak of $\text{C}=\text{O}$ in $-\text{COOH}$ at 1702 cm^{-1} shifted to 1716 cm^{-1} . In addition, the asymmetric stretching vibration of $-\text{COO}-$ at 1635 cm^{-1} also shifted to 1654 cm^{-1} . The stretch vibration peak that belongs to $\text{O}=\text{C}=\text{O}-$ at 1557 cm^{-1} slightly shifted to 1560 cm^{-1} . Apart from this, the characteristic peak split to 1541 and 1550 cm^{-1} . It proves that the carboxylic acid (COOH or COO-Li^+) in the PAA interacted with CCA to form the hydrogen bonds or strong dipole bonding between CCA molecular and PAA polymer chains.⁴¹

Figure 6 shows (a) and (c) CV and (b) and (d) voltage profile of anodes made of (a) and (b) Si flakes and (c) and (d) CCA-coated silicon flakes (Si@CA) for revealing the electrochemical reactions of the battery during charging and discharging. The lower part of the CV represents the reduction and the upper part the oxidation reactions. Figure 6a shows the CV curve of the first three cycles of discharge–charge of the as-received Si anode. Figure 6c shows the CV curve of the first three cycles of the Si@CA anode.

The reduction reactions of the Si@CA anode exhibit a typical CV curve. After the first cycle of discharge, the crystalline silicon flakes change to amorphous silicon. After the first cycle of charge and discharge is completed, a reduction

peak appears at about 0.18 V. This peak is due to the phase conversion during the reaction process. In the process of transforming amorphous silicon to Li_xSi , the reduction peak increases significantly with the number of charging–discharging cycles. In the oxidation curve, there are oxidation peaks at about 0.36 and 0.52 V, which reflect the decomposition of Li_xSi to form amorphous silicon. The peaks of the oxidation curve increase significantly with the number of charging–discharging cycles, indicating strong reactions.

Figure 6b shows the voltage profiles of the first 3 cycles and the 10th cycle of the as-received Si anode. The discharge capacity of the first cycle of silicon reached about 3300 mAh/g, and the ICE was about 82%. The discharge capacity decreased to about 2210 mAh/g after 10 cycles. Figure 6d shows the voltage profiles of the first 3 cycles and the 10th cycle of the Si@CA anode. The CCA coating serves as a protective layer for silicon. The specific capacity of this electrode is about 3259 mAh/g. The specific capacity is measured as per gram of CCA-coated silicon. The proportion of the CCA carbon shell is around 3.5–4.5 wt %. CCA coating effectively protected the silicon from reacting with the electrolyte and improved the ICE to 88.3%. In addition, the CCA coating provides mechanical support to silicon flakes and reduces the structural damages caused by the volume changes of the silicon during charging and discharging. It effectively slows down the cycling capacity degradation in the later stage.

Figure 7a shows specific capacity cycling performance of anodes made of (1) (blue) silicon flakes and (red) Si@CA. The charging–discharging current for the first three cycles is 0.2 A/g, and after that, the cycling test is performed at the current of 1 A/g. The mass loading of all three sets of samples is 1.5 mg/cm². The ICE of the as-received Si electrode is 80.5%. After the silicon flakes are encapsulated by CCA coating, the ICE increased significantly to 88.3%.

The CCA coating is terminated by COOH groups that form hydrogen bonds with the –COO– groups on the surrounding PAA binder. In addition, the CCA coating provides mechanical support for the coated silicon particles to reduce the possibility of structural damages caused by the volume changes of silicon during discharging and charging. This makes Si@CA perform better in the later stage of cycling.

The specific capacity of the as-received Si anode is 1300 mAh/g (per gram of silicon flakes) after 200 cycles in comparison with 1500 mAh/g (per gram of CCA-coated silicon flakes) for Si@CA after 200 cycles of discharge–charge. The mass loadings of both two samples are 1.5 mg/cm². The CA carbon shell effectively protects the silicon powder at the beginning of the cycling and prevents the silicon flakes from deteriorating in the subsequent cycles. A high areal capacity of more than 1.6 mAh/cm² was retained after the 200th charging and discharging cycle. The Coulomb efficiency is about 99.7–99.8% after 200 times of cycling.

Figure 7b shows cycling performance of as-received silicon flakes and Si@CA at discharge–charge current ranging from 0.2 A/g (0.05 C) to 4 A/g (0.96 C). Silicon flakes without CCA coating lack sufficient electrical conductivity and perform poorly at the high charge–discharge current of 4 A/g. A low specific capacity of <150 mAh/g was achieved at 4 A/g for the anode made of silicon flakes without CCA coatings. With CCA coatings, the specific capacitance retains above 1000 mAh/g. When the discharge–charge current is restored to 0.2 A/g, the specific capacity of as-received Si and Si with CCA coatings (Si@CA) recovered to 2700 and 2500 mAh/g, respectively,

indicating that there were not severe damages to the anode by the high current of 4 A/g discharge–charge cycling of both anodes.

Figure 7c shows electrochemical impedance spectra of the first cycle Si and Si@CA anode and the curve fitting equivalent circuit, where R1 represents the bulk resistance, (R2, CP1) and (R3, CP2) are the equivalent diffusion impedance, and W the Warburg element. R1, R2, and R3 obtained from curve fitting are shown in Table 1. It shows that CCA coating reduces both

Table 1. Equivalent Circuit Parameters Obtained from Curve Fitting of Electrochemical Impedance Spectra Shown in Figure 7c

	Si flake	Si flake@CA
R1 (Ω)	9	6
R2 (Ω)	30	18
R3 (Ω)	24	20

the charge transfer resistance (R3) in the intermediate frequency region and the diameter of the overall semicircles. The charge transfer resistance decreases with the increasing amount of CA additive. The slopes of the low frequency region of the EIS curves are similar, indicating that they have similar lithium-ion diffusion rates.^{42,43}

Figure 8 shows SEM images of the anode surface made with as-received silicon flakes shown in Figure 8a,b and silicon

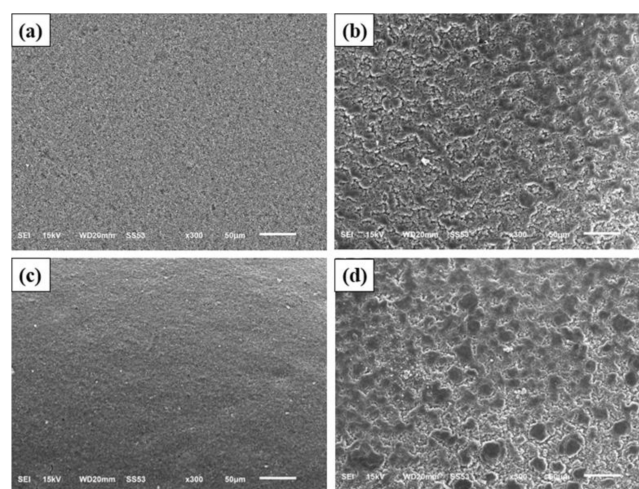


Figure 8. SEM images of the anode surface made with (a, b) as-received silicon flakes and (c, d) silicon flakes with carbonized CA coating (Si@CA) (a, c) before and (b, d) after the 200th discharge–charge cycle.

flakes with CCA coating (Si@CA) shown in Figure 8c,d and before and after the 200th discharge–charge cycle, as shown in Figure 8a,c and Figure 8b,d, respectively. Figure 8a,b show SEM images of the anode made of as-received silicon flakes before and after charging and discharging cycling, respectively. Figure 8c,d shows SEM images of the Si@CA anode before and after charging and discharging cycling, respectively. Figure 8d shows fewer cracks on the surface of the Si@CA electrode after cycling than what is shown in Figure 8b for silicon without CCA coatings. The chemical and physical protection of the CCA layer for silicon contributes to the superior physical integrity of the Si@CA electrode. The CCA buffer layer not only prevents direct contact between the silicon

powder and the electrolyte, but also promote uniform lithiation and de-lithiation processes, which is desirable for reducing the internal stresses of silicon and deformation of the electrode during cycling. As a result, good physical integrity was achieved and no large-scale cracks were found on the surface of the anodes after 200 cycles of discharge–charge.

Table S1 compares the ICE and the specific capacity of some selected silicon-based anodes, which were recently published with this work. S1–7: PAA binder results in improved ICE, S1, S6 when compared with other binders shown in Table S1. The Si@CA with PAA binder from this work was demonstrated to be the best performing anode with both the highest ICE of 88.3% and good capacity retention of 1479 mAh/g after 200 cycles of discharge–charge. The coating of CCA improves both the ICE and the high-current (4 A/g) discharge–charge cycling performance of the silicon-flake-based anode using PAA as a binder. Strong interfacial affinity between the PAA binder and Si@CA provides excellent physical integrity of the micron-sized silicon flakes and the anode structure, resulting in overall electrochemical performance being superior to anodes made of more expensive nano-silicon powder. S2–S4: The additional electrical conductivity provided by CCA further improves the capability of the anode in high-current discharge–charge. A facile fabrication process has been reported using economic micron-sized silicon flakes to demonstrate superior anode performance for LIB.

Additional data are included in the Supporting information. Figure S1 shows results of a thermogravimetric analysis of Si and Si@CA. Figure S2 shows electrochemical impedance spectral of the Si anode and Si@CA anode after 200 cycles of discharge–charge. Figure S3 shows Raman spectra of CA and CCA. Figure S4 shows (i) SEM images of anode surfaces made of silicon flake and CCA-coated silicon flake after cycling, (ii) elemental analysis of anode surfaces after cycling, and (iii) voltage profile of anodes.

4. CONCLUSIONS

A durable high-ICE silicon-based LIB anode capable of high discharge–charge current has been fabricated by a facile process using an inexpensive micron-sized silicon flakes recycled from silicon semiconductor industry. PAA binder was applied to firmly bond together silicon flakes, which were coated with CCA to enhance electrical conductivity and minimize pulverization of silicon flakes and cracks in the anode due to volume changes. COOH functional groups on both PAA and CCA form strong bonds. High ICE, around 90%, and retention of 1500 mAh/g capacity were achieved after 200 discharge–charge cycles at 1 A/g. Even at a higher current density of 4 A/g, retention of 1000 mAh/g capacity was achieved. The combined effects of conductivity enhancement and the strong bonding between the PAA binder with CCA-coated silicon flake overcome technical barriers in low electrical conductivity and up to about 400% volume changes of silicon due to alloying with lithium in a modern silicon-based anode. Excellent physical integrity and electrochemical performance of a silicon-based anode for LIB have been demonstrated.

■ ASSOCIATED CONTENT

SI Supporting Information

The Supporting Information is available free of charge at <https://pubs.acs.org/doi/10.1021/acsomega.2c07830>.

Comparisons of initial coulombic efficiency and specific capacity of selected high performance anodes, thermogravimetric analysis of Si and Si@CA, electrochemical impedance spectral measurements of the Si anode and Si@CA anode after 200 cycles of discharge–charge, Raman spectra of CA and CCA, SEM images of anode surfaces made of silicon flake and carbonized CA-coated silicon flake after cycling, elemental analysis of anode surfaces after cycling, and voltage profile of the anode, and references (PDF)

■ AUTHOR INFORMATION

Corresponding Author

Yonhua Tzeng – Institute of Microelectronics, Department of Electrical Engineering, College of Electrical and Computer Engineering, National Cheng Kung University, Tainan 701, Taiwan; orcid.org/0000-0003-4763-1144; Email: tzengyo@mail.ncku.edu.tw

Authors

Cheng-Ying Jhan – Institute of Microelectronics, Department of Electrical Engineering, College of Electrical and Computer Engineering, National Cheng Kung University, Tainan 701, Taiwan

Guan-Yu Chen – Institute of Microelectronics, Department of Electrical Engineering, College of Electrical and Computer Engineering, National Cheng Kung University, Tainan 701, Taiwan

Kuo-Ming Chiu – Institute of Microelectronics, Department of Electrical Engineering, College of Electrical and Computer Engineering, National Cheng Kung University, Tainan 701, Taiwan

Yi-Chen Wu – Institute of Microelectronics, Department of Electrical Engineering, College of Electrical and Computer Engineering, National Cheng Kung University, Tainan 701, Taiwan

Pin-Sen Wang – Institute of Microelectronics, Department of Electrical Engineering, College of Electrical and Computer Engineering, National Cheng Kung University, Tainan 701, Taiwan

Complete contact information is available at: <https://pubs.acs.org/doi/10.1021/acsomega.2c07830>

Author Contributions

Y.T.: Conceptualization, methodology, validation, formal analysis, investigation, writing—original draft preparation, supervision, and funding acquisition. C.-Y.J.: Methodology, validation, formal analysis, investigation, and writing—original draft preparation. K.-M.C.: Validation, formal analysis, investigation, and writing—original draft preparation. Y.-C.W.: Validation, formal analysis, and investigation. G.-Y.C.: Validation, formal analysis, and investigation. P.-S.W.: Validation, formal analysis, investigation, and writing—original draft preparation.

Funding

This work is partially supported by the Ministry of Science and Technology in Taiwan under the grant number MOST-111-2221-E-006-155.

Notes

The authors declare no competing financial interest.

ACKNOWLEDGMENTS

The authors gratefully acknowledge the use of the scanning electron microscope (Hitachi-SU8000, Taipei, Taiwan), the ultrahigh resolution transmission electron microscope (STEM JEOL-2100F CS, Taipei, Taiwan), and elemental analyzer (UNICUBE) equipment provided by the Instrument Center of National Cheng Kung University.

REFERENCES

- (1) Scrosati, B.; Garche, J. Lithium batteries: Status, prospects and future. *J. Power Sources* **2010**, *195*, 2419–2430.
- (2) Thackeray, M. M.; Wolverton, C.; Isaacs, E. D. Electrical energy storage for transportation—approaching the limits of, and going beyond, lithium-ion batteries. *Energy Environ. Sci.* **2012**, *5*, 7854–7863.
- (3) Li, Z.; Huang, J.; Liaw, B. Y.; Metzler, V.; Zhang, J. A review of lithium deposition in lithium-ion and lithium metal secondary batteries. *J. Power Sources* **2014**, *254*, 168–182.
- (4) Zhang, W.-J. A review of the electrochemical performance of alloy anodes for lithium-ion batteries. *J. Power Sources* **2011**, *196*, 13–24.
- (5) Wu, H.; Cui, Y. Designing nanostructured Si anodes for high energy lithium ion batteries. *Nano Today* **2012**, *7*, 414–429.
- (6) Kasavajjula, U.; Wang, C.; Appleby, A. J. Nano- and bulk-silicon-based insertion anodes for lithium-ion secondary cells. *J. Power Sources* **2007**, *163*, 1003–1039.
- (7) McDowell, M. T.; Lee, S. W.; Nix, W. D.; Cui, Y. 25th anniversary article: understanding the lithiation of silicon and other alloying anodes for lithium-ion batteries. *Adv. Mater.* **2013**, *25*, 4966–4985.
- (8) Liu, X. H.; Zhong, L.; Huang, S.; Mao, S. X.; Zhu, T.; Huang, J. Y. Size-dependent fracture of silicon nanoparticles during lithiation. *ACS Nano* **2012**, *6*, 1522–1531.
- (9) Kim, H.; Seo, M.; Park, M. H.; Cho, J. A critical size of silicon nano-anodes for lithium rechargeable batteries. *Angew. Chem., Int. Ed.* **2010**, *49*, 2146–2149.
- (10) Rahman, M. A.; Song, G.; Bhatt, A. I.; Wong, Y. C.; Wen, C. Nanostructured silicon anodes for high-performance lithium-ion batteries. *Adv. Funct. Mater.* **2016**, *26*, 647–678.
- (11) Arico, A. S.; Bruce, P.; Scrosati, B.; Tarascon, J.-M.; Van Schalkwijk, W. Nanostructured materials for advanced energy conversion and storage devices. In *Materials for sustainable energy: a collection of peer-reviewed research and review articles from Nature Publishing Group: World Scientific*, 2011; pp 148–159.
- (12) Son, Y.; Sim, S.; Ma, H.; Choi, M.; Son, Y.; Park, N.; Park, M. Exploring Critical Factors Affecting Strain Distribution in 1D Silicon-Based Nanostructures for Lithium-Ion Battery Anodes. *Adv. Mater.* **2018**, *30*, No. 1705430.
- (13) Yoo, J. K.; Kim, J.; Jung, Y. S.; Kang, K. Scalable fabrication of silicon nanotubes and their application to energy storage. *Adv. Mater.* **2012**, *24*, 5452–5456.
- (14) Chan, C. K.; Peng, H.; Liu, G.; McIlwrath, K.; Zhang, X. F.; Huggins, R. A.; Cui, Y. High-performance lithium battery anodes using silicon nanowires. *Nat. Nanotechnol.* **2008**, *3*, 31–35.
- (15) Xin, S.; Wu, Q.; Li, J.; Xiao, X.; Lott, A.; Lu, W.; Brian, W.; Wu, J. Silicon-based nanomaterials for lithium-ion batteries: a review. *Adv. Energy Mater.* **2014**, *4*, No. 1300882.
- (16) Ge, M.; Fang, X.; Rong, J.; Zhou, C. Review of porous silicon preparation and its application for lithium-ion battery anodes. *Nanotechnology* **2013**, *24*, No. 422001.
- (17) Cook, J. B.; Kim, H.-S.; Lin, T. C.; Robbennolt, S.; Detsi, E.; Dunn, B. S.; Tolbert, S. H. Tuning porosity and surface area in mesoporous silicon for application in Li-ion battery electrodes. *ACS Appl. Mater. Interfaces* **2017**, *9*, 19063–19073.
- (18) Shia, Q.; Zhou, J.; Ullaha, S.; Yangab, X.; Tokarskac, K.; Trzebickac, B.; Quang, H.; Rummeli, T. M. H. A review of recent developments in Si/C composite materials for Li-ion batteries. *Energy Storage Mater.* **2021**, *34*, 735–754.
- (19) Luo, W.; Chen, X.; Xia, Y.; Chen, M.; Wang, L.; Wang, Q.; Li, W.; Yang, J. Surface and interface engineering of silicon-based anode materials for lithium-ion batteries. *Adv. Energy Mater.* **2017**, *7*, No. 1701083.
- (20) An, W.; He, P.; Che, Z.; Xiao, C.; Guo, E.; Pang, C.; He, X.; Ren, J.; Yuan, G.; Du, N.; Yang, D.; Peng, D.-L.; Zhang, Q. Scalable Synthesis of Pore-Rich Si/C@C Core-Shell-Structured Microspheres for Practical Long-Life Lithium-Ion Battery Anodes. *ACS Appl. Mater. Interfaces* **2022**, *14*, 10308–10318.
- (21) Lanhui, G.; Han, J.; Chen, M.; Zhou, W.; Wang, X.; Xu, M.; Lin, H.; Liu, H.; Chen, H.; Chen, J.; Zhang, Q.; Han, X. Enabling robust structural and interfacial stability of micron-Si anode toward high-performance liquid and solid-state lithium-ion batteries. *Energy Storage Mater.* **2022**, *52*, 547–561.
- (22) Shi, J.; Jiang, X.; Sun, J.; Ban, B.; Li, J.; Chen, J. Recycled silicon-based anodes with three-dimensional hierarchical porous carbon framework synthesized by a self-assembly CaCO₃ template method for lithium ion battery. *J. Alloys Compd.* **2021**, *858*, No. 157703.
- (23) Tzeng, Y.; Jhan, C.-Y.; Yi-Hsuan, W. Effects of Pyrolysis on High-Capacity Si-Based Anode of Lithium Ion Battery with High Coulombic Efficiency and Long Cycling Life. *Nanomaterials* **2022**, *12*, 469.
- (24) Tzeng, Y.; Jhan, C.-Y.; Wu, Y.-C.; Chen, G.-Y.; Chiu, K.-M.; Yang-En, S. High-ICE and High-Capacity Retention Silicon-Based Anode for Lithium-Ion Battery. *Nanomaterials* **2022**, *12*, 1387.
- (25) Dong, Z.; Wubin, D.; Yan, C.; Zhang, C.; Chen, G.; Chen, J.; Sun, W.; Jiang, Y.; Liu, Y.; Gao, M.; Gan, J.; Yang, Y.; Pan, H. A novel tin-bonded silicon anode for lithium-ion batteries. *ACS Appl. Mater. Interfaces* **2021**, *13*, 45578–45588.
- (26) Luo, F.; Feng, X.; Zeng, L.; Lin, L.; Li, X.; Kang, B.; Xiao, L.; Chen, Q.; Wei, M.; Qian, Q. In situ simultaneous encapsulation of defective MoS₂ nanolayers and sulfur nanodots into SPAN fibers for high rate sodium-ion batteries. *Chem. Eng. J.* **2021**, *404*, No. 126430.
- (27) Xu, L.; Chen, X.; Guo, W.; Zeng, L.; Yang, T.; Xiong, P.; Chen, Q.; Zhang, J.; Wei, M.; Qian, Q. Co-construction of sulfur vacancies and carbon confinement in VSS8/CNFs to induce an ultra-stable performance for half/full sodium-ion and potassium-ion batteries. *Nanoscale* **2021**, *13*, 5033–5044.
- (28) Ke, C.; Shao, R.; Zhang, Y.; Sun, Z.; Qi, S.; Zhang, H.; Li, M.; Chen, Z.; Wang, Y.; Sa, B.; Lin, H.; Liu, H.; Wang, M.-S.; Chen, S.; Zhang, Q. Synergistic engineering of heterointerface and architecture in new-type ZnS/Sn heterostructures in situ encapsulated in nitrogen-doped carbon toward high-efficient lithium-ion storage. *Adv. Funct. Mater.* **2022**, *32*, No. 2205635.
- (29) Zeng, L.; Fang, Y.; Xu, L.; Zheng, C.; Yang, M.-Q.; He, J.; Xue, H.; Qian, Q.; Wei, M.; Chen, Q. Rational design of few-layer MoSe₂ confined within ZnSe–C hollow porous spheres for high-performance lithium-ion and sodium-ion batteries. *Nanoscale* **2019**, *11*, 6766–6775.
- (30) Han, X.; Zhou, W.; Chen, M.; Chen, J.; Wang, G.; Liu, B.; Luo, L.; Chen, S.; Zhang, Q.; Shi, S.; Wong, C.-P. Interfacial nitrogen engineering of robust silicon/MXene anode toward high energy solid-state lithium-ion batteries. *J. Energy Chem.* **2022**, *67*, 727–735.
- (31) Buqa, H.; Holzapfel, M.; Krumeich, F.; Veit, C.; Novák, P. Study of styrene butadiene rubber and sodium methyl cellulose as binder for negative electrodes in lithium-ion batteries. *J. Power Sources* **2006**, *161*, 617–622.
- (32) Nguyen, C. C.; Yoon, T.; Seo, D. M.; Guduru, P.; Lucht, B. L. Systematic investigation of binders for silicon anodes: interactions of binder with silicon particles and electrolytes and effects of binders on solid electrolyte interphase formation. *ACS Appl. Mater. Interfaces* **2016**, *8*, 12211–12220.
- (33) Cai, Z. P.; Liang, Y.; Li, W. S.; Xing, L. D.; Liao, Y. H. Preparation and performances of LiFePO₄ cathode in aqueous solvent with polyacrylic acid as a binder. *J. Power Sources* **2009**, *189*, 547–551.
- (34) Magasinski, A.; Zdyrko, B.; Kovalenko, I.; Hertzberg, B.; Burtovyy, R.; Huebner, C. F.; Fuller, T. F.; Luzinov, I.; Yushin, G.

Toward efficient binders for Li-ion battery Si-based anodes: polyacrylic acid. *ACS Appl. Mater. Interfaces* **2010**, *2*, 3004–3010.

(35) Tian, M.; Chen, X.; Sun, S.; Dong, Y.; Wu, P. A bioinspired high-modulus mineral hydrogel binder for improving the cycling stability of microsized silicon particle-based lithium-ion battery. *Nano Res.* **2019**, *12*, 1121–1127.

(36) Dong, Y.; Shao, J.; Chen, C.; Li, H.; Wang, R.; Chi, Y.; Lin, X.; Chen, G. Blue luminescent graphene quantum dots and graphene oxide prepared by tuning the carbonization degree of citric acid. *Carbon* **2012**, *50*, 4738–4743.

(37) Kikuchi, K.; Yamamoto, K.; Nomura, N.; Kawasaki, A. Synthesis of n-type Mg₂Si/CNT thermoelectric nanofibers. *Nanoscale Res. Lett.* **2017**, *12*, 343.

(38) Hossain, S.; Johra, F. T.; Jung, W.-G. Fabrication of silicon carbide from recycled silicon wafer cutting sludge and its purification. *Appl. Sci.* **2018**, *8*, 1841.

(39) Delpuech, N.; Mazouzi, D.; Dupre, N.; Moreau, P.; Cerbelaud, M.; Bridel, J. S.; Badot, J. C.; De Vito, E.; Guyomard, D.; Lestriez, B.; Humbert, B. Critical role of silicon nanoparticles surface on lithium cell electrochemical performance analyzed by FTIR, Raman, EELS, XPS, NMR, and BDS spectroscopies. *J. Phys. Chem. C* **2014**, *118*, 17318–17331.

(40) Liu, Y.; Zhao, C.; Sabirsh, A.; Ye, L.; Wu, X.; Lu, H.; Liu, J. A Novel Graphene Quantum Dot-Based mRNA Delivery Platform. *ChemistryOpen* **2021**, *10*, 666–671.

(41) Anyu, S.; Pang, Q.; Chen, X.; Dong, J.; Zhao, Y.; Lian, R.; Dong, Z.; Liu, B.; Chen, G.; Wei, Y. Lithium poly-acrylic acid as a fast Li⁺ transport media and a highly stable aqueous binder for Li₃V₂(PO₄)₃ cathode electrodes. *J. Mater. Chem. A* **2018**, *6*, 23357–23365.

(42) Guo, J.; Sun, A.; Chen, X.; Wang, C.; Manivannan, A. Cyclability study of silicon–carbon composite anodes for lithium-ion batteries using electrochemical impedance spectroscopy. *Electrochim. Acta* **2011**, *56*, 3981–3987.

(43) Suh, S.; Yoon, H.; Park, H.; Kim, J.; Kim, H.-J. Enhancing the electrochemical performance of silicon anodes for lithium-ion batteries: One-pot solid-state synthesis of Si/Cu/Cu₃Si/C electrode. *Appl. Surf. Sci.* **2021**, *567*, No. 150868.